Spatiotemporal Hysteresis Distribution and Decomposition of Solar Activities and Climatic Oscillation during 1900–2020

Mingyang Li[1], Tingxi Liu[1,*], Long Ma[1,*], Limin Duan[1], Yixuan Wang[1], Guoqiang Wang[2], Huimin Lei[3], Vijay Singh[4]

[1] Inner Mongolia Water Resource Protection and Utilization Key Laboratory; Water Conservancy and Civil Engineering College, Inner Mongolia Agricultural University, Hohhot 010018, China;

[2] College of Water Sciences, Beijing Normal University, Beijing 100875, China;

[3] State Key Laboratory of Hydroscience and Engineering, Department of Hydraulic Engineering, Tsinghua University, Beijing 100084, China;

[4] Department of Biological and Agricultural Engineering & Zachry Department of Civil Engineering, Texas A& M University, College Station, TX 77843, USA).

Corresponding author: Tingxi Liu (txliu1966@163.com)

Long Ma (838276345@qq.com)

Key Points:

- Two distinct dividing lines in the hysteresis distribution of T and P respectively
- MHDM descript how lag of SA to T & P decomposed into CO, SY & GF
- Weight distribution of SA, GF and CO in RGB false color synthesis

Abstract

Meteorological elements have different lag periods for solar activities (SA), climatic oscillation (CO) and other influencing factors at different spatiotemporal scales. To further understand the "solar-climate-water resource" system, this study considers China as the study area and investigates the monthly data of temperature (T) and precipitation (P) during 1900–2020 that were obtained from 3836 grid stations. The strong interaction and lag distribution between T or P with SA and CO were studied and influence weights of SA, CO, and geographical factors (GF) of each grid station were calculated. A multivariate hysteretic decomposition model was established to simulate and quantitatively decompose the periodic lag considering the factors of the earth's revolution. The results indicate the existence of two dividing lines in the distribution of T and P lag periods. Additionally, the underlying surface conditions and urbanisation were observed to have significant effects on the periodic lag of meteorological elements.

1 Introduction

Air temperature (T) and precipitation (P) are the primary indicators reflecting the climatic characteristics of a region and the key factors influencing the ecohydrological cycle and balanced exchange of water and heat (Chen et al., 2021b; Li et al., 2020; Song and Wu, 2021). Both T and P exhibited relatively unique variation and distribution patterns in different spatiotemporal scales (Zhang, 2021). They display distinct periodic characteristics due to astronomical and terrestrial factors such as solar activities (SA), planetary positions of the sun and earth, climatic oscillation of the earth (CO) and zonal characteristics due to geographical factors (GF) such as latitude and longitude, terrain level, and underlying surface properties (Chen et al., 2021a; Nan et al., 2021; Wood et al., 2020). The processes and mechanisms of different influencing factors on individual components of hydrothermal balance vary; this variation causes different lag periods in the responses of T and P in different regions (Huang et al., 2020; Yetemen et al., 2019). The coupling effect of numerous factors requires thorough investigation to enable better understanding of the "sun-earth climate-water resource" system, quantitative simulation and calculation of the coupling relationships of components, accurate prediction of extreme climatic changes. Additionally, understanding the factors and their effects can also help in ensuring improved and rapid responses to climatic changes.

SA refers to various active phenomena in local areas of the solar atmosphere, primarily caused by electromagnetic processes in the solar atmosphere (Friis-Christensen and Lassen, 1991). These phenomena include occurrence of sunspots, light spots, spectral spots, flares, prominences, and activities in the corona. SA has an average cycle of 11.2 a (Wilcox, 1976) and has been associated with earthquakes, volcanic eruptions, droughts, floods, and even diseases of the human cardiac and nervous systems (Marchitelli et al., 2020). Sunspot numbers (SN) are caused by strong magnetic field activity of the sun that inhibit convection, cooling the surface and giving an appearance of a relatively darker colour to the region, which are the most common and prominent of all SAs.

The effects of SN on the Earth's climate garnered increasing interest in the early 20th century. However, the investigations had certain limitations; some focused on a single site, such limitations prevented a comprehensive understanding of the effects of SN, while others had a short study duration. Since the 1990s, relevant studies have improved on spatiotemporal scales; however, the accuracy of the surface scale studies and regional representation remain poor. Investigations are primarily stagnated at the macro discussion and comparison levels (Friis-Christensen and

Lassen, 1991; Haigh, 1996). With the frequent occurrence of extreme weather events, studies after the 21st century have become more extensive in both quantity and content (Brehm et al., 2021; De la Torre et al., 2007; Li et al., 2018b; Ramanathan et al., 2001; Ramanathan and Feng, 2009; Xu et al., 2021). According to the aforementioned studies, SN, as an important indicator representing SA, can explain the hysteresis effect of T and P. However, due to the partial consideration of factors, the results of these studies are limited to the fixed law of the lag period, such as the change of the position relationship between the sun and the earth caused by the revolution of the earth, CO; other key elements are not included in the model or analysis.

CO refers to a statistically significant change or long-term change in climate state due to natural or anthropogenic factors, which reflects the climatic state of small regions and small basins, and is affected by SA and other aspects (Nishikawa et al., 2021). Southern Oscitation Index (SOI) and Sea Surface Temperature (SST) are two important indicators reflecting CO (Abtew et al., 2009; Namadi and Deng, 2021). Both represent the interaction and equilibrium process of the atmospheric and oceanic coupling system and can more carefully describe the abnormal phenomena such as El Nino, La Nina and Ramadre (Du et al., 2020; Kamruzzaman et al., 2020; Kang et al., 2019). Existing studies that have investigated the influence of CO on regional T or P space focused on the spatial distribution law, instead of the distribution law of lag, and the studies considering SA and CO are even less rare. In terms of the specific influencing factors, most of studies have explored the influence or lag effect qualitatively through the statistical law; however, only a few studies established mathematical or mechanism model for quantitative research. Moreover, most of studies are conducted on a small scale in terms of regional selection and few cross-climatic zones (Dikshit et al., 2021).

This study used the data of raster weather stations in China collected during 1900–2020 and the data of SA and CO in long-time series (Figure 1). The time series law and spatial distribution characteristics of all indicators under long-time series were investigated. The periodic and hysteresis effects of SA and CO on T and P of China were analysed under six periodic scales. Based on the comprehensive consideration of the earth's revolution process, a multivariate hysteresis decomposition (MHD) model was proposed and established. We regrouped the study area according to the weight of influential factors, quantitatively decomposed the contribution of factors affecting the lag of T and P, and simulated the lag period.

Figure 1 Schematic diagram of regional temperature and precipitation under the combined influence of solar activity and climatic oscillation.

2 Materials and Methods

2.1 Study area

The research area corresponds to the People's Republic of China (73°33' -135 °05' E, 3°51' -53 °33' N), located in the east of Asia and the west coast of the Pacific Ocean. The overall terrain is high in the west and low in the east, with a ladder distribution and a vast area of mountains and plateaus. China can be divided into the northern region, the southern region, and the Qinghai–Tibet Plateau region according to the 400 mm annual isohyet and the boundary line of the first and second terrains. The overall monsoon climate is significant. During the same period of rain and heat, the southern region is dominated by subtropical and tropical monsoon climates, the northern region is dominated by temperate monsoon and continental climate, and the Qinghai–Tibet Plateau

region presents plateau mountain climate (Supplementary Figure S1). The research area and the network of 0.5 × 0.5° raster weather stations used are shown in Figure 2.

Figure 2 Map of the study region indicating the locations of the 3836 monthly global grid high-resolution stations.

2.2 Method and model

This study divides the research period into six periodic scales, namely, short (0–5 and 5–10 a), medium (10–30 and 30–60 a), and long (60–90 and 90–120 a), based on the overall analysis of time series rule. The T and P data from 3836 grid meteorological stations across China were used to study the cross and SN, SOI, and SST influence and lag time and space distribution analysis; the results were combined with the site location, lag effect, and revolution of the earth to establish an MHD model, dismantling and quantify various time scales in China's T and P a lag effect mechanism (Figure 3).

Figure 3. Flowchart showing the derivation of datasets from the data on daily T, P, SN, SOI, and SST, and their interaction mechanism. SN: sunspot number; SOI: southern oscillation index; SST: NINO 3.4 sea surface temperature.

2.2.1 Regulation and cross influence analysis

Discrete Fourier Transform (DFT) is used to transform time series from time to frequency domain for T and P, SN, SOI, and SST data; then, the data structure and variation regulation of time series were studied. The cross influence of T and P monthly data of 3836 grid meteorological stations, spatiotemporal distribution analysis of SN, SOI, and SST, and lag were calculated using the cross-wavelet transform (Taghizadeh-Mehrjardi et al., 2021) and the wavelet type was Morlet. Within the 95% confidence interval of the six periodic scales, we extracted the period represented by the most intense value of power from the wavelet power spectrum and the condensed spectrum respectively as the period of interaction or lag between the station and the corresponding elements. In the spatial and temporal distribution of strong interaction and lag period, if there are multiple peaks in the series of temporal numbers under a time scale, we consider the maximum value as the result of the station under this periodic scale. In the calculation of the lag period, 1/2 of the periodic scale is taken as the zero point, the co-direction phase relation is taken as positive, and the reverse phase relation is taken as negative. In order to facilitate the mapping and analysis of the lag distribution, the reverse phase relation is rotated 1/2 of the period to be taken as positive. Under a large periodic scale, there will be a long pseudo-lag (pseudo-interaction) period, which we call superimposed lag (interaction) period.

2.2.2 Regulation and cross influence analysis

The variation of time series of meteorological elements is affected by long-term trends, seasonal, and irregular variations. To eliminate random factors in the data, we used seasonal-trend decomposition based on loess (STL) to smooth the data (Figure 4a, b). The STL method is a time series decomposition method with both generality and robustness. It is characterised by self-control of trend, smoothness of periodic components, and good robustness to outliers.

There is an auto cross correlation of a meteorological element and itself at different time points. We used autocorrelation function to conduct autocorrelation analysis on T and P data of

each grid meteorological stations. The time delay coefficient is obtained through the self-covariance, namely, the self-delay period of this element (SY), which can be used for the subsequent quantitative separation of elements in the MDH model (Figure 4c, d).

Figure 4. The original, seasonal, trend and residual terms of T (a) and P (b) by seasonal and trend decomposition using loess method (STL) and the autocorrelation using the residual terms of T (c) and P (d) by STL. Graph shows the data preprocessing of the sample grid station of China, and this method is applied to all station data used in the study.

2.2.3 MDH model

In order to explore the interaction relationship and mutual feed mechanism among meteorological elements in the SA-CO region, based on the hysteresis period of T and P of each grid station, we decomposed the hysteresis period of SA on meteorological elements into the influence of SA on CO, as well as the transformation of CO, GF, including longitude, latitude, and elevation), solar altitude angle (SEA for short, θ in model) caused by the revolution of the earth and meteorological element SY. The aforementioned decomposition factor relations is expressed in Figure 3 and Eq. 1.

$$A = \alpha_1 A' + f(B, C) + \mathrm{g}(Lat, Lon, Alt) + \alpha_2 D + \delta \quad (1)$$

$$f(B, C) = \tau_1 B \times tan\theta + \tau_2 C_1 + \tau_3 C_2 \quad (2)$$

$$\mathrm{g}(Lat, Lon, Alt) = \rho_1 Lat + \rho_2 Lon + \rho_3 Alt \quad (3)$$

where, A, B, C, D represent the hysteresis period of the SA to meteorological elements, the solar to climate, the CO to local meteorology and the SY period of meteorological factors, respectively. A' is the strong action of SA on meteorological elements. C can be divided into C_1 and C_2, which respectively represent the period of hysteresis effect and strong action of SA on CO. θ is SEA. α_1, α_2, α_3 are the hysteresis adjustment coefficient of the earth's climate, GF, and SY, respectively; τ_1, τ_2, τ_3 are the influence parameters of the SA on the climate and the CO on local meteorological conditions; ρ_1, ρ_2, ρ_3 are the hysteresis response parameters of GF (latitude, longitude, and elevation) to meteorological elements, respectively; δ is the regulating parameter of the solar - CO - local meteorological hysteresis model.

During the earth's revolution, the angle of incidence of sun's rays on the earth changes, which determines the amount of solar heat received by the earth surface. The SEA at the locations of grid meteorological stations in the study area is used to represent the influence of the earth at different positions in the orbit, which can be calculated by Eq. 4.

The SEA varies with local time, local latitude, and the sun declination, and can be expressed as:

$$sin\theta = sin\sigma \times sin\varphi + cos\sigma \times cos\varphi \times cost \quad (4)$$

where, the declination of the sun (latitude equal to the point of direct sunlight) is expressed by σ; the geographic latitude of the observation site is expressed by φ (both solar declination and geographic latitude are positive in the north latitude and negative in the south latitude); and the local time (hour angle) is expressed by t.

186 2.2.4 Entropy weights method

187 Entropy is a measure of the disorder of a system. According to the definition of information
188 entropy, for a certain index, the entropy value can be used to judge the degree of dispersion of an
189 index. The smaller the information entropy value is, the greater the degree of dispersion of the
190 index will be, and the greater the influence (i.e. weight) of the index on the comprehensive
191 evaluation will be. If all the values of an index are equal, the index has no effect in the
192 comprehensive evaluation. Therefore, the tool of information entropy can be used to calculate the
193 weight of each index and provide a basis for the comprehensive evaluation of multiple indexes.
194 We standardized the data of each index. Given *k* indices X_1, X_2, ... , X_k, where

195 $$X_i = \{x_1, x_2, \cdots, x_n\} \quad (5)$$

196 Assume that the normalized value of all index data are $\{Y_1, Y_2, \cdots, Y_n\}$. We can get

197 $$Y_{ij} = \frac{X_{ij} - min(X_i)}{max(X_i) - min(X_i)} \quad (6)$$

198 The information entropy of a set of data can be defined as:

199 $$E_j = -\frac{1}{\ln n}\sum_{i=1}^{n} p_{ij} \ln p_{ij} \quad (7)$$

200 where, $p_{ij} = Y_{ij} / \sum_{i=1}^{n} Y_{ij}$. If $p_{ij} = 0$, we define $\lim_{p_{ij} \to 0} p_{ij} \ln p_{ij} = 0$. According to the calculation
201 formula of information entropy, the information entropy of each index is calculated as
202 $\{E_1, E_2, \cdots, E_n\}$. The weight of each index is calculated by information entropy:

203 $$W_i = \frac{1 - E_j}{k - \sum E_i} \ (i = 1,2, \cdots, k) \quad (8)$$

204 2.2.5 Hysteresis area grouping and model evaluation index

205 K-means clustering, which is popular for cluster analysis in data mining, aims to partition
206 n observations into K-clusters in which each observation belongs to the cluster with the nearest
207 mean, serving as a prototype of the cluster. At each grid station, the influence entropy weights of
208 SA, CO and GF are grouped into 6 groups, which respectively represent the scenario in which the
209 two of the three influence factors have the highest weight ratio.

210 *p* values were used to test the sample variance of the measured and the simulated values,
211 and the significance level was set to 0.05. When the *p* value was less than 0.01, there was a highly
212 significant statistical difference. We use the coefficient of determination (R^2) and the root-mean-
213 square error (RMSE) to evaluate the lag (superimposed lag) period of MDH model simulation.
214 They are defined as follows:

215 $$R^2 = 1 - \frac{RSS}{TSS} \quad (9)$$

216 $$RMSE = \sqrt{\frac{\sum_{t=1}^{n} (I_p - I_o)^2}{n}} \quad (10)$$

217 where RSS is the residual sum of squares; TSS is the total sum of squares; I_p and I_o are the
218 observed and predicted lag (superimposed lag) period (a), respectively; and n is the total simulation
219 number.

3 Data

The research data includes the monthly T and P data of 3836 raster weather stations from 1900 to 2020, the index SN of SA, the monitoring index SOI and Nino 3.4 SST of CO, and the digital elevation model (DEM) of the location of the raster weather stations in the research area (Table 1). Among them, "Udel_airt_precip" data is used for data from 1900 to 2017 (Willmott and Matsuura, 2001), and data interpolation from China's national meteorological stations is used for data from 2018 to 2020.

Table 1. Utilized information and number of T, N, SN, SOI, SST, SEA and DEM data in the research. T: air temperature; P: precipitation; SN: sunspot number; SOI: southern oscillation index; SST: NINO 3.4 sea surface temperature; SEA: solar elevation angle; DEM: digital elevation model.

4 Results

4.1 Periodic distribution of T and P

The periodic distribution of T in China at the scale of 0–5 a is similar to that in climatic zones. T has a significant period of 6–8 a between 25° N and 45° N on the scale of 5–10 a. On the scale of 10–30 a, the significant period of T increased step-by-step from east to west, and increases in the region to the west of 80° E (Figure 5a).

Compared with T, the periodic distribution of P is more scattered and patchier, which is mainly manifested in the 2–4 a period of the central and eastern part of China at the scale of 0–5 a, and the 1 a period of the Qinghai–Tibet region in the northwest of China. At 5–30 a scale, the significant period of P in Northeast, North, and East China was approximately 8–14 a. The P significant period in the northwest of Mount Qomolangma at the 5–90 a scale slightly varies from that in the Qinghai–Tibet region, and it mainly exhibits significant periods at 7.5, 34 and 88 a (Figure 5b). The obtained results are consistent with the results of Sun et al. (2017) that were obtained using the national meteorological stations data in China to study the spatial heterogeneity and annual distribution of T and P.

Figure 5. Grided, latitude and longitude scale distribution of (a) T and (b) P periodicity of China under six periodic scales (1900–2020).

4.2 Periodic distribution of T and P

In terms of periodicity, SN is extremely active during 7.3–16.1 a, with an average cycle length of 11.2 a. There is a century cycle of SA in 80–90 a, with 3 or 4 consecutive 11.2 a significant peaks followed by 3 or 4 consecutive 11.2 a low peaks (Figure 6a). The most significant regulation of SOI sequence is 1 a; the 2.5 a cycle is also significant (Figure 6b). A substantial proportion of the energy fluctuations of SST in Nino3.4 region were primarily distributed in the period 1 a and 2–7 a. There is a significant period of 9–14 years from 1970 to 2015 (Figure 6c). According to the cross-wavelet analysis of SN, SOI, and SST (Figure 6d–g), a significant interaction between SA and CO mainly occurs in the periods of 0.25, 0.5, 1 a and 8–16 a.

Figure 6. Continuous wavelet spectra of SN, SOI and SST (a-c). Cross wavelet transforms and wavelet coherences between SN and SOI (d, f), SST (e, g). (The thin solid line represents the wavelet influence cone, the thick solid line represents the horizontal interval of 5 % significance,

the right arrow represents the concentric phase relationship, and the left arrow represents the inverse phase relationship.)

4.3 Interaction period distribution

The periodic distribution of strong interaction between SN, T, and P was consistent with significant high correlation periods of 1.03, 11.02 and 83.21 a. The significant superposition interaction periods were 9.82, 55.53 and 88.15 a. On the scale of 10–30 a, T in northern China exhibited a significant high correlation period of 9.82 years. Furthermore, on the 0–5 a scale, the precipitation in some areas of Northwest China displayed a significant high correlation period of 4.63 a (Supplementary Figure S2a, b; Supplementary Table S1).

The strong interaction periods of SOI and Nino3.4 SST against T and P were consistent with those observed in the study area. The results indicated periods of significant high correlation between CO and T at 1.03, 11.02 and 83.21 a. The significant superposition interaction periods were 9.27, 9.82, 55.53, 58.84 and 88.15 a. On the 10–30 a scale, the strong interaction period of T in the northwest, southwest and north of China was relatively large. On the 60–90 a scale, the strong interaction period of T in Northeast China and South China was relatively small. The strong interaction period of P was relatively high in the 10–30 a scale in Northeast China (Supplementary Table S2).

Compared with T, the strong interaction period distribution of CO and P indicated patchier characteristic, and the second significant high correlation periods were primarily 1.09, 2.45 (Southeast and Northwest China), 11.67, 24.73 (Northeast China and along the Kunlun Mountains), 44.07 (Central and South China), 58.84 a (patch distribution), etc. (Supplementary Figure S2c–f).

4.4 Hysteresis period distribution

Overall, the periodic hysteresis characteristics of T to SN and CO were concentrated at 0–5 a and 60–120 a scales in spatial distribution, whereas the patchiness of P was more significant. The main lag response periods of T to SA were 0.24–0.63, 1.03–3.58, and 4.55–10.78 a (Supplementary Table S3); the superimposed lag periods included 21.34–24.84, 57.79–65.11, and 66.28–69.91 a (Figure 7a). Additionally, on the 0–5 a scale, the lag period in eastern region was slightly longer than that of the western region by 0.1–0.2 a. On the 5–10 a scale, the hysteretic response period of North China, East China and Central China was slightly shorter, ranging from 0.57 to 1.29 a. On the scale of 60–120 a, the superimposed hysteresis period of Tarim Basin, Tanggula Mountain and Sichuan Basin was significant.

The primary lag response periods of T to CO were 0.25–0.54, 1.39–4.08, and 6.25–7.25 a (Supplementary Table S4); the superimposed lag periods included 9.74–12.82, 24.91–29.36, 56.27–61.89, and 65.78–69.64 a (Figure 7c, e). Moreover, on the 5–10 a scale, the hysteretic response period of Northwest, Northeast, and East China was slightly shorter. On the scale of 10–30 a, the P hysteresis response period in the eastern region was longer. On the 60–120 a scale, there were two distinct superimposed hysteresis dividing lines in the east and west respectively: the Central Gobi–Ordos Plateau–Hengshan–Yanshan Mountains, and the southern foot of the northern Tibetan Plateau–Chechen River–Turpan Basin.

The main hysteresis response cycles of P to SN were 0.25–0.54, 1.39–4.08, and 5.20–7.10 a (Supplementary Table S3); the superimposed hysteresis cycles included 11.91–18.72, 21.85–25.36, and 48.99–59.43 a (Figure 7b). On the 10–30 a scale, the hysteresis period of North China

and Northern Central China was slightly longer. On the 30–60 a scale, the hysteresis period of northeast, southeast and western regions was relatively short, which is 30.87–37.87 a. The main lag response period of P to CO was similar to that of T, but the distribution characteristics were different (Figure 7d, f). On the 5–10 a scale, the hysteresis period of Northeast China and Sichuan Basin was relatively short. On the 10–30 a scale, the superimposed hysteresis period of Northeast China and the eastern part of the Qinghai–Tibet Plateau was slightly longer. On the scale of 60–120 a, P also contained two distinct superimposed hysteresis cycle dividing lines: The Greater Hinggan—Taihang—Wushan–Xuefeng Mountains and the Qilian—Bayankla–Hengduan Mountains.

Figure 7. The significant lag period distributions of SN (a, b), SOI (c, d) and SST (e, f) to T and P of China under six periodic scales (The significance level = 0.95).

4.5 Analysis of influencing factors

To further study the effects of SA, CO, and GF on the T and P periodic hysteresis in China, the entropy weight method was employed to analyse the contribution weight of the hysteresis effect of grid stations over 121 years. We used false colour synthesis to facilitate observation. The influence weight of SA corresponds to the intensity of red in the RGB channel, whereas CO and GF correspond to blue and green respectively (Figure 8). The results indicated that the weights of periodic lag factors of T and P have distinct geographical boundaries that are consistent with the boundaries of lag effects of T and P at the scale of 60–120 a.

GF is an important factor affecting the lag of T and P in China. The periodic lag of T is significantly affected by SA and CO in Northeast, Northern North, and Western Northwest China. The periodic lag of P is highly affected by SA and CO in the central and northern regions of China; furthermore, it is highly affected by SA and GF in the Sichuan basin and the upstream region of the Yellow River.

Figure 8. Entropy weight of SA, CO, and regional GF to the periodic hysteresis of T (a) and P (b) under six periodic scales in China. Red, blue, and green represent SA, CO, and GF, respectively (significance level = 0.95).

4.6 Geographical partition of influencing factors

Clustering k-means was used to divide 3836 grid meteorological stations in the research area into six groups according to the influence weights of SA, CO, and GF on the T and P periodic lag in China. These groups corresponded to the arrangement and combination of the weights of the three influencing factors (Supplementary Figure S3), to facilitate the decomposition of MHD model and the simulation of the lag effect of meteorological elements. The results demonstrated that the weight clustering partition retained the delay effect boundary. The western and northeastern mountains of China form their own groups in the lagged grouping of T. The Northeast Plain and the Inner Mongolia Plateau were combined into a group, similar to the grouping used for the Loess Plateau, Sichuan Basin and Yunnan–Guizhou Plateau. The lag group of P was similar to the terrain trend. The northeast plain and surrounding mountains were divided into two groups, while the eastern coastal plain and mountain areas were separated.

4.7 Quantitative simulation of lag effects

The strong interaction period, lag effect period and solar altitude angle (SEA) of the six periodic scales generated above were respectively substituted into MHD model in groups according to the weights of the six influencing factors to simulate the lag period of the study area under different periodic scales. The model parameters and accuracy error analysis are detailed in Supplementary Table S5 and Figure 9. The results indicated that the overall effect of MHD model in splitting and simulating the T hysteresis effect was better than that of P. For regions below 40° N, the T lag simulation R^2 of the model was between 0.6–0.95. The interpretation degree was not high in Northeast and North China, and several regions with error values >10 a were scattered in Northwest and Southwest China. The accuracy and error of P lag simulations in East, South, and South-Central China were excellent; although, the simulation error in North China was low, the interpretation degree was not high. The model had a high degree of interpretation for the Himalayas, Qinghai Lake, and southern Taiwan province, but the error of the six periods was large (Figure 9).

Figure 9. Accuracy (a, b) and error (c, d) analysis of simulated T (a, c) and P (b, d) hysteresis period distribution using multivariate hysteretic decomposition model (MHD model; Eq.1). RMSE: root mean squared error (The significance level = 0.95).

5 Discussion

5.1 Hysteretic response mechanism and pseudo-cycle

According to the fluctuation characteristics of meteorological elements, SA, and CO in the same time domain, it was observed that T and P have the same variation period in multiple time-frequency domains (Huang et al., 2020; Li et al., 2018a; Yetemen et al., 2019). In addition to the interannual period (1.03 a), the interaction between T and P and SN and CO was prominently strong at the SA and Glasberg periods of 9–13 a (average 11.2 a) and 80–90 a (average 87 a), respectively. There was also a strong interaction between the middle part of the research area and CO with a 21–25 a Haier cycle (average 22 a) (Supplementary Figure S2). The hysteresis response cycles are more abundant in spatiotemporal scales. The hysteresis (superposition hysteresis) cycles included interannual, SA, and Haier cycles; moreover, they were significant in 3–6 and 64–70 a cycles.

Although, both T and P have hysteresis effect on the fluctuation of SA and CO in the long-time scale, it was observed that in the same region, long interaction/hysteresis period can be obtained by combining short interaction/hysteresis period with the length of SA period. For example, under the interaction period of 90–120 a, the significant period of 88.15 a can be perfectly decomposed into 4 11.02 a (Supplementary Table S1, S2). The superimposed significant lag period of precipitation at the scale of 60–90 a is a multiple of the sum of two small significant lag periods at the scale of 0–5 and 5–10 a (Supplementary Figure S4). Even the lag close to the SA cycle can be decomposed into 2–3 significant lag cycles at the 5–10 a scale (Supplementary Table S3, S4). Previous studies suggest that the spatial lag of meteorological elements can be understood as the combined result of many individual event responses (Kamruzzaman et al., 2020; Namadi and Deng, 2021) and illustrate the importance of identifying true and false cycles in studying interaction/hysteresis processes.

5.2 Analysis of interaction lag distribution and influence effect

For a long periodic scale (60–120 a), the periodic correlation distribution of SN and CO to T or P is the same in the entire study area. The results suggest that the effects of SA and CO on T or P have mutual effects of assimilation across topographical and climatic zones, and the assimilation can be understood as the geographical homogenisation of climatic elements. The strong interaction distribution results indicate that SOI and Nino3.4 SST have the same influence on the lag period distribution of regional T and P, suggesting that the influence of CO on regional meteorological elements, introduces consistency in the CO index in the region (van der Kaars et al., 2010).

The distribution pattern of strong interaction and lag periods exhibited distinct geographical division at various scales, and the regional boundaries of different intensities and periods were approximately consistent with the intense fluctuation of terrain. The lag periods of T and P and the dividing line of the pattern of influencing factors can be divided into the east line and the west line, both of which are reflected in the strong interaction and periodic lag response. The T lag dividing lines run through water veins or valleys where mountains meet, and the gaps in the mountains facilitate the cross-regional flow of monsoons. The P lag dividing lines are the zones of drastic terrain change, where the high mountains block the transport of water vapour. Considering the average lag period of seven regions in China for comparison, it was found that the northern region of China has the longest lag period, and the lag period of surrounding regions tends to converge to the northern region. The lag period caused by SN in Southwest China is greater than that in Northwest China, while the lag effect of CO is opposite for the aforementioned two regions (Figure 10a-b). The lagging trend of precipitation also has similar characteristics, except that the central part of China has the longest lag period (Figure 10c-d).

Figure 10. Theoretical diagram of the variation of (a, b) T and (c, d) P on the hysteresis period distribution of (a, c) SN and (b, d) CO. NW: Northwest China; N: North China; SW: Southwest China; E: Eastern China; C: Central China; S: South China.

The lag spatial distribution of T and P shows that it is nested with the terrain (Brunner et al., 2021) and echoes with the city (Marelle et al., 2020). Additionally, abrupt topographical changes within distinct boundaries, such as those in the Tarim Basin in western China also affect the lag spatial distribution. Based on the hysteresis effect on T, it can be deduced that the northern Tarim Basin is the region where GF has great influence. For P, SA has a significant effect on the Taklimakan Desert, south of Tarim Basin.

Regional underlying surface conditions and anthropogenic activities are also important factors affecting T and P periodic lag (Wood et al., 2020), which is particularly reflected in the patchy distribution of P period lag. According to the weighting factors of the influence of P in the decomposition, there are two dominant area that are mainly affected by SA and GF (Figure 5b slant yellow area), are primarily distributed in the Loess Plateau, the northeast and the Yunnan–Guizhou plateau, Maowusu sandy land; the areas respectively correspond to the two major rivers, the bend of Yellow River and the middle and upper reaches of Yangtze river (Yibin–Three gorges). In this instance, GF can provide more information on underlying surface (Brunner et al., 2021; Wei et al., 2021). The patchy lag distribution of P is also significantly related to anthropogenic activities such as urbanisation (Marelle et al., 2020; Zhang et al., 2021).

5.3 Hysteresis decomposition and uncertainty analysis

From the simulation results, it can be understood that there remains a substantial scope for improvement in the disassembly and simulation of hysteresis effect (Figure 9). According to the obtained results, urbanisation has a significant impact on the periodic lag distribution of P. In this study, the weights of three influencing factors, SA, CO, and GF, were classified and clustered, which met the zoning requirements of surface scale (Michniewicz et al., 2020). However, for P, a meteorological element with conspicuous patchiness, it was targeted to a greater extent at the group level by adding urbanisation level indicators (Marelle et al., 2020), such as proportion of land for construction and urbanisation level, which may substantially improve the control of P characteristics (Du et al. 2020).

Furthermore, the consideration of influencing factors and method of decomposition of factors increase the uncertainty levels in the study. Influencing factors of the uncertainty of both celestial, space weather (such as the gravitational pull of the moon and interference of the interplanetary magnetic field) may affect the propagation process of solar energy in space (Zheng et al., 2019), including the earth itself (such as ocean currents and volcanic eruptions), and directly or indirectly alter the local climate (Marchitelli et al., 2020). The decomposition of the influencing factors can also be improved. Regardless of the scope of physical or semi-physical improvement in the connection between the components according to the influencing mechanism, a refined geographical division and larger spatiotemporal scale are conducive to the effective analysis of the hysteresis response of meteorological factors to SA and CO.

6 Conclusions

In this study, we investigated the periodicity of T and P in China over 121 years from 1900 to 2020 on six periodic scales. the strong interaction period with SA and CO and the hysteresis effect on them was also studied. The weight distribution of factors influencing T and P periodic hysteresis in China was plotted, and the hysteresis responses of T and P to SA, CO, and GF were quantified and simulated by MHD model.

The results indicate that T and P have a similar variation period in multiple time-frequency domains and a distinct strong interaction and lag or superposition lag period in interannual, SA, Haier, and Glassberg cycles. The long superposition interaction/hysteresis period can be divided into several short interaction/hysteresis periods. The periodic distribution of strong interaction and lag indicates that they are nested with the terrain and correspond with the city at a distance. Additionally, the underlying surface conditions and urbanisation are important factors affecting the periodic hysteresis of T and P. There are two distinct dividing lines in the lag period of T and P and the pattern of influencing factors, respectively. The dividing lines of T are between mountains and valley terrain, that include the Central Gobi–Ordos Plateau–Hengshan–Yanshan and the southern foot of the northern Tibetan Plateau–Cherchen River–Turpan Basin. The dividing lines of P correspond to the zone of sharp terrain change that include the Greater Hinggan—Taihang—Wushan–Xuefeng Mountains and Qilian—Bayankela–Hengduan Mountains.

Acknowledgments, Samples, and Data

This research was funded by the National Natural Science Foundation of China (Nos. 51939006 and 51620105003), the National Key R&D Program of China (No. 2018YFC0406400), the Inner

Mongolia Science and Technology Plan Project (No. 2020), the Ministry of Education Innovative Research Team (No. IRT_17R60), the Inner Mongolia Industrial Innovative Research Team (No. 2012), the Natural Science Foundation of Inner Mongolia Autonomous Region of China (No. 2020JQ06), the Inner Mongolia Major science and technology projects (No. 2019ZD007). Thanks for the UDel_AirT_Precip data provided by the NOAA/OAR/ESRL PSL, Boulder, Colorado, USA, from their Web site at https://www.psl.noaa.gov/data/gridded/data.UDel_AirT_Precip.html. Thanks for the cross wavelet and wavelet coherence software provided by A. Grinsted. (C) Aslak Grinsted 2002-2014 http://www.glaciology.net/wavelet-coherence.Thanks for the Sunspot Index and Long-term Solar Observations data belongs to the Royal Observatory of Belgium (hereinafter "ROB"), from their Web site at http://sidc.oma.be/silso/monthlyssnplot. Thanks for the Southern Oscillation Index (SOI) data belongs to the Bureau of Meteorology, from their Web site at http://www.bom.gov.au/climate/current/soi2.shtml. All generated methods used in this study can be downloaded from https://github.com/myli1993/T-P-response-to-SA-CO. And generated data can be downloaded from https://pan.baidu.com/s/101t-wgtWa31Pf85J-VXO3A and the extract code is TPSA. There are no conflicts of interest to declare.

References

Abtew W., Melesse A.M., Dessalegne T. (2009) El Nino Southern Oscillation link to the Blue Nile River Basin hydrology. Hydrological Processes 23:3653-3660. DOI: 10.1002/hyp.7367.

Brehm N., Bayliss A., Christl M., Synal H.A., Adolphi F., Beer J., Kromer B., Muscheler R., Solanki S.K., Usoskin I., Bleicher N., Bollhalder S., Tyers C., Wacker L. (2021) Eleven-year solar cycles over the last millennium revealed by radiocarbon in tree rings. Nature Geoscience 14:10-+. DOI: 10.1038/s41561-020-00674-0.

Brunner M.I., Swain D.L., Gilleland E., Wood A.W. (2021) Increasing importance of temperature as a contributor to the spatial extent of streamflow drought. Environmental Research Letters 16:10. DOI: 10.1088/1748-9326/abd2f0.

Chen C., Chen Q.W., Li G., He M.N., Dong J.W., Yan H.L., Wang Z.Y., Duan Z. (2021a) A novel multi-source data fusion method based on Bayesian inference for accurate estimation of chlorophyll-a concentration over eutrophic lakes. Environmental Modelling & Software 141:12. DOI: 10.1016/j.envsoft.2021.105057.

Chen F.H., Duan Y.W., Hou J.Z. (2021b) An 88 ka temperature record from a subtropical lake on the southeastern margin of the Tibetan Plateau (third pole): new insights and future perspectives. Science Bulletin 66:1056-1057. DOI: 10.1016/j.scib.2021.02.031.

De la Torre L., Gimeno L., Anel J.A., Nieto R. (2007) The role of the solar cycle in the relationship between the, North Atlantic Oscillation and Northern Hemisphere surface temperatures. Advances in Atmospheric Sciences 24:191-198. DOI: 10.1007/s00376-007-0191-x.

Dikshit A., Pradhan B., Alamri A.M. (2021) Long lead time drought forecasting using lagged climate variables and a stacked long short-term memory model. Science of the Total Environment 755:12. DOI: 10.1016/j.scitotenv.2020.142638.

Du Y.H., Berndtsson R., An D., Zhang L.N., Yuan F.F., Hao Z.C. (2020) Integrated large-scale circulation impact on rainy season precipitation in the source region of the Yangtze River. International Journal of Climatology 40:2285-2295. DOI: 10.1002/joc.6332.

Friis-Christensen E., Lassen K. (1991) Length of the solar cycle: an indicator of solar activity closely associated with climate. Science (New York, N.Y.) 254:698-700. DOI: 10.1126/science.254.5032.698.

Haigh. (1996) The Impact of Solar Variability on Climate. Science (New York, N.Y.) 272:981-4. DOI: 10.1126/science.272.5264.981.

Huang X., Ma L., Liu T.X., Sun B.L., Zhou Y., Yang C., Qiao Z.X. (2020) Spatial and temporal variability of the abrupt interannual temperature change and warming hiatus in China, 1951-2016. Meteorological Applications 27:17. DOI: 10.1002/met.1911.

Kamruzzaman M., Metcalfe A., Beecham S. (2020) Modelling spatial and temporal rainfall and their relationship to climatic indicators in South Australia. Theoretical and Applied Climatology 142:543-553. DOI: 10.1007/s00704-020-03314-0.

Kang N.Y., Kim D., Elsner J.B. (2019) The contribution of super typhoons to tropical cyclone activity in response to

515 ENSO. Scientific Reports 9:6. DOI: 10.1038/s41598-019-41561-y.
516 Li M.K., Zhang S.Q., Wu L.X., Lin X.P., Chang P., Danabasoglu G., Wei Z.Q., Yu X.L., Hu H.Q., Ma X.H., Ma W.W.,
517 Jia D.N., Liu X., Zhao H.R., Mao K., Ma Y.W., Jiang Y.J., Wang X., Liu G.L., Chen Y.H. (2020) A high-
518 resolution Asia-Pacific regional coupled prediction system with dynamically downscaling coupled data
519 assimilation. Science Bulletin 65:1849-1858. DOI: 10.1016/j.scib.2020.07.022.
520 Li W., Duan L.M., Luo Y.Y., Liu T.X., Scharaw B. (2018a) Spatiotemporal Characteristics of Extreme Precipitation
521 Regimes in the Eastern Inland River Basin of Inner Mongolian Plateau, China. Water 10. DOI: ARTN 35
522 10.3390/w10010035.
523 Li Z., Yue J.P., Xiang Y.F., Chen J., Bian Y.K., Chen H.Q. (2018b) Multiresolution Analysis of the Relationship of
524 Solar Activity, Global Temperatures, and Global Warming. Advances in Meteorology 2018:8. DOI:
525 10.1155/2018/2078057.
526 Marchitelli V., Troise C., Harabaglia P., Valenzano B., De Natale G. (2020) On the Long Range Clustering of Global
527 Seismicity and its Correlation With Solar Activity: A New Perspective for Earthquake Forecasting. Frontiers
528 in Earth Science 8:8. DOI: 10.3389/feart.2020.595209.
529 Marelle L., Myhre G., Steensen B.M., Hodnebrog O., Alterskjaer K., Sillmann J. (2020) Urbanization in megacities
530 increases the frequency of extreme precipitation events far more than their intensity. Environmental Research
531 Letters 15:9. DOI: 10.1088/1748-9326/abcc8f.
532 Michniewicz A., Jancewicz K., Migon P. (2020) Large-scale geomorphological mapping of tors - Proposal of a key
533 and landform interpretation. Geomorphology 357:12. DOI: 10.1016/j.geomorph.2020.107106.
534 Namadi P., Deng Z.Q. (2021) Modeling and Forecasting Vibrio Parahaemolyticus Concentrations in Oysters. Water
535 Research 189:11. DOI: 10.1016/j.watres.2020.116638.
536 Nan S.L., Zhao P., Chen J.M., Liu G. (2021) Links between the thermal condition of the Tibetan Plateau in summer
537 and atmospheric circulation and climate anomalies over the Eurasian continent. Atmospheric Research
538 247:15. DOI: 10.1016/j.atmosres.2020.105212.
539 Nishikawa S., Wakamatsu T., Ishizaki H., Sakamoto K., Tanaka Y., Tsujino H., Yamanaka G., Kamachi M., Ishikawa
540 Y. (2021) Development of high-resolution future ocean regional projection datasets for coastal applications
541 in Japan. Progress in Earth and Planetary Science 8:22. DOI: 10.1186/s40645-020-00399-z.
542 Ramanathan V., Crutzen P.J., Kiehl J.T., Rosenfeld D. (2001) Aerosols, climate, and the hydrological cycle. Science
543 (New York, N.Y.) 294:2119-24. DOI: 10.1126/science.1064034.
544 Ramanathan V., Feng Y. (2009) Air pollution, greenhouse gases and climate change: Global and regional perspectives.
545 Atmospheric Environment 43:37-50. DOI: 10.1016/j.atmosenv.2008.09.063.
546 Song L., Wu R. (2021) Two Types of Rossby Wave Breaking Events and Their Influences on East Asian Winter
547 Temperature. Journal of Geophysical Research-Atmospheres 126. DOI: 10.1029/2020jd033917.
548 Taghizadeh-Mehrjardi R., Schmidt K., Toomanian N., Heung B., Behrens T., Mosavi A., Band S.S., Amirian-Chakan
549 A., Fathabadi A., Scholten T. (2021) Improving the spatial prediction of soil salinity in arid regions using
550 wavelet transformation and support vector regression models. Geoderma 383:21. DOI:
551 10.1016/j.geoderma.2020.114793.
552 van der Kaars S., Tapper N., Cook E.J. (2010) Observed relationships between El Nino-Southern Oscillation, rainfall
553 variability and vegetation and fire history on Halmahera, Maluku, Indonesia. Global Change Biology
554 16:1705-1714. DOI: 10.1111/j.1365-2486.2009.02025.x.
555 Wei X.T., Huang S.Z., Huang Q., Leng G.Y., Wang H., He L., Zhao J., Liu D. (2021) Identification of the interactions
556 and feedbacks among watershed water-energy balance dynamics, hydro-meteorological factors, and
557 underlying surface characteristics. Stochastic Environmental Research and Risk Assessment 35:69-81. DOI:
558 10.1007/s00477-020-01896-9.
559 Wilcox J.M. (1976) Solar structure and terrestrial weather. Science (New York, N.Y.) 192:745-8. DOI:
560 10.1126/science.192.4241.745.
561 Willmott C.J., Matsuura K. (2001) Terrestrial Air Temperature and Precipitation: Monthly and Annual Time Series
562 (1950 - 1999). http://climate.geog.udel.edu/~climate/html_pages/README.ghcn_ts2.html.
563 Wood T., Maycock A.C., Forster P.M., Richardson T.B., Andrews T., Boucher O., Myhre G., Samset B.H., Kirkevag
564 A., Lamarque J.F., Muelmenstaedt J., Olivi D., Takemura T., Watson-Parris D. (2020) The Southern
565 Hemisphere Midlatitude Circulation Response to Rapid Adjustments and Sea Surface Temperature Driven
566 Feedbacks. Journal of Climate 33:9673-9690. DOI: 10.1175/jcli-d-19-1015.1.
567 Xu T., Zhu L., Ma Q., Wang J., Lu X., Tang L. (2021) Moisture and vegetation variations in the extremely cold-dry
568 area of the Tibetan Plateau during the past 5000 years. Catena 204. DOI: 10.1016/j.catena.2021.105381.
569 Yetemen O., Saco P.M., Istanbulluoglu E. (2019) Ecohydrology Controls the Geomorphic Response to Climate
570 Change. Geophysical Research Letters 46:8852-8861. DOI: 10.1029/2019gl083874.

Zhang J.Z. (2021) Global patterns of phosphorus transformation in relation to latitude, temperature and precipitation. Pedosphere 31:214-220. DOI: 10.1016/s1002-0160(20)60063-7.

Zhang X.Z., Chen J.Z., Song S.F. (2021) Divergent impacts of land use/cover change on summer precipitation in eastern China from 1980 to 2000. International Journal of Climatology 41:2360-2374. DOI: 10.1002/joc.6963.

Zheng Y.H., Ganushkina N.Y., Jiggens P., Jun I., Meier M., Minow J.I., O'Brien T.P., Pitchford D., Shprits Y., Tobiska W.K., Xapsos M.A., Guild T.B., Mazur J.E., Kuznetsova M.M. (2019) Space Radiation and Plasma Effects on Satellites and Aviation: Quantities and Metrics for Tracking Performance of Space Weather Environment Models. Space Weather-the International Journal of Research and Applications 17:1384-1403. DOI: 10.1029/2018sw002042.

[Data] Bureau of Meteorology. Southern Oscillation Index (SOI) data; http://www.bom.gov.au/climate/current/soi2.shtml.

[Data] Royal Observatory of Belgium. Sunspot Index and Long-term Solar Observations data; http://sidc.oma.be/silso/monthlyssnplot.

[Data] Willmott C J and Matsuura K. Terrestrial Air Temperature and Precipitation: Monthly and Annual Time Series (1950 - 1999). 2001; http://climate.geog.udel.edu/~climate/html_pages/README.ghcn_ts2.html.

[Data] University of Delaware Air Temperature & Precipitation. https://www.psl.noaa.gov/data/gridded/data.UDel_AirT_Precip.html

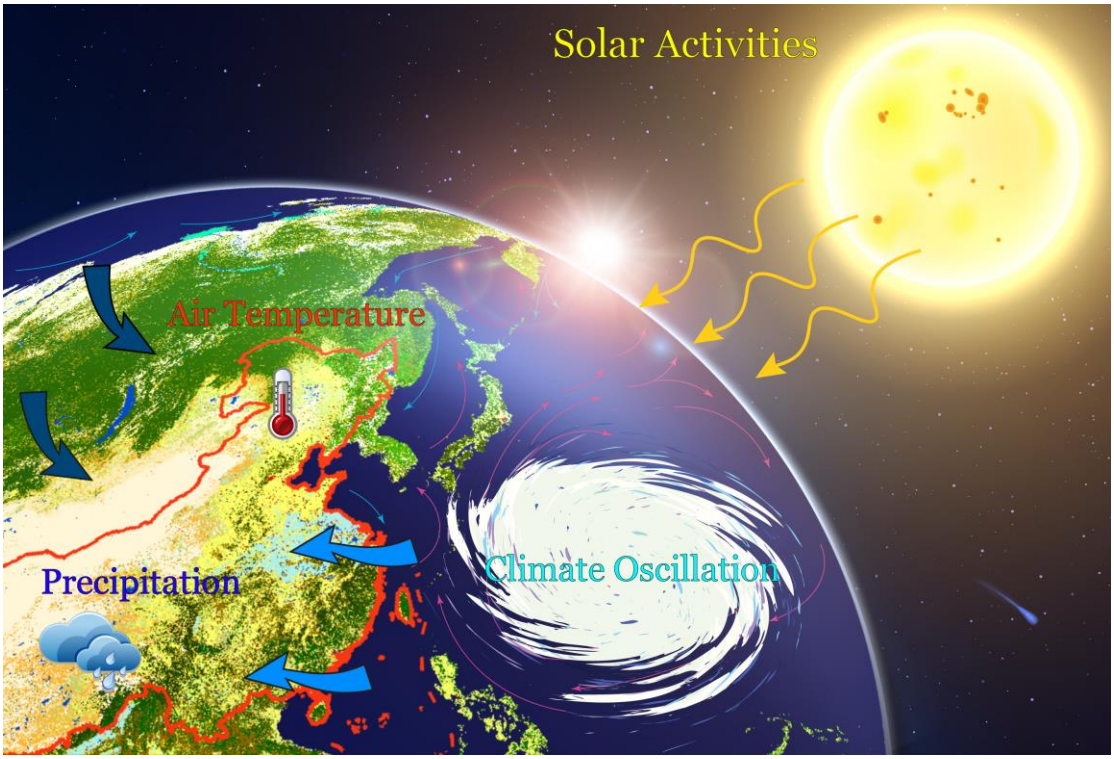

Figure 1. Schematic diagram of regional temperature and precipitation under the combined influence of solar activity and climatic oscillation.

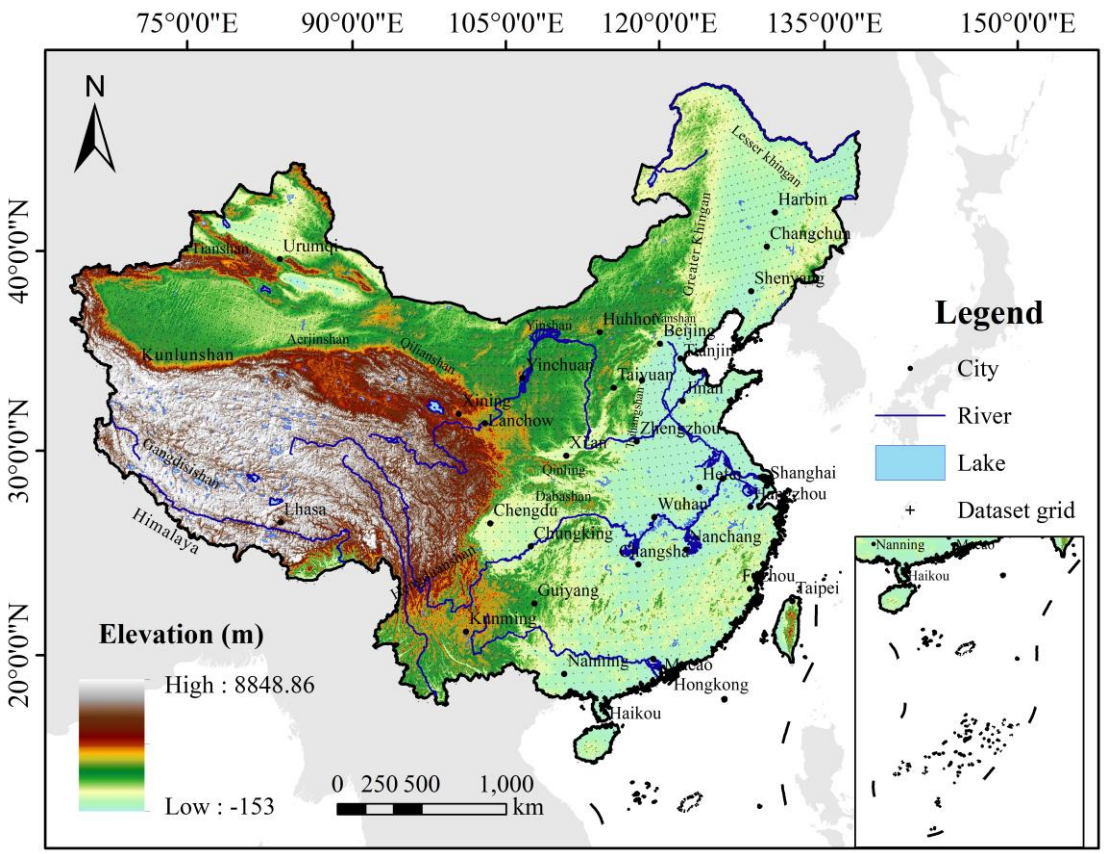

Figure 2. Map of the study region indicating the locations of the 3836 monthly global grid high-resolution stations.

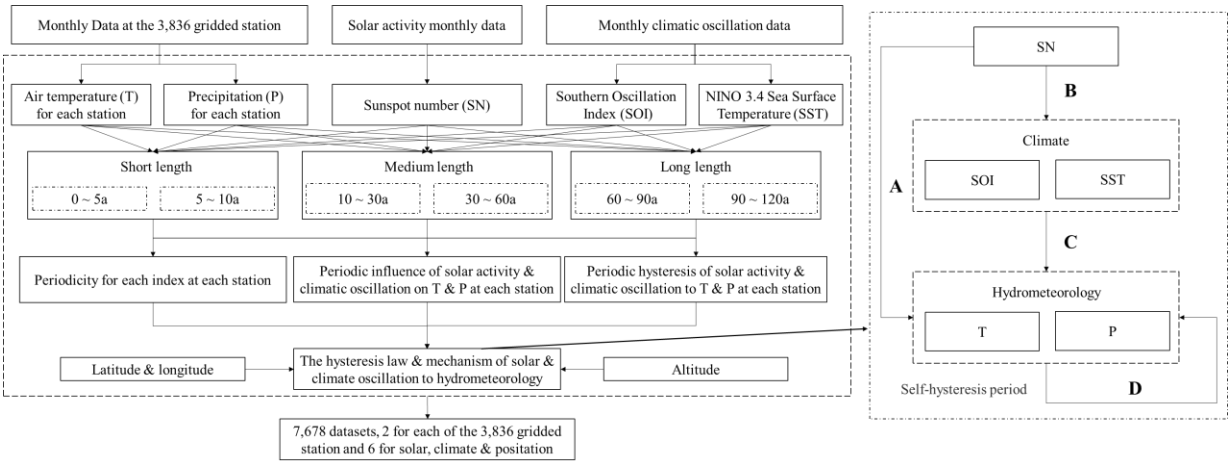

Figure 3. Flowchart showing the derivation of datasets from the data on daily T, P, SN, SOI, and SST, and their interaction mechanism. SN: sunspot number; SOI: southern oscillation index; SST: NINO 3.4 sea surface temperature.

602

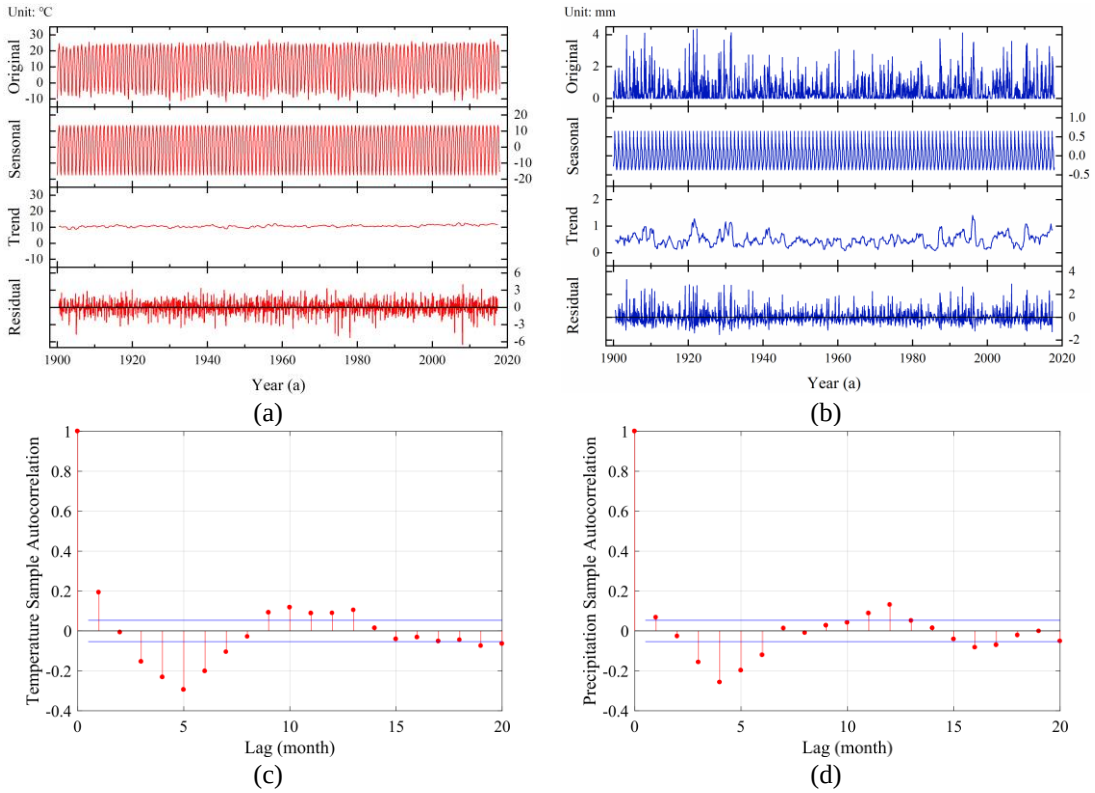

603 **Figure 4**. The original, seasonal, trend and residual terms of T (a) and P (b) by seasonal and trend
604 decomposition using loess method (STL) and the autocorrelation using the residual terms of T (c)
605 and P (d) by STL. Graph shows the data preprocessing of the sample grid station of China, and
606 this method is applied to all station data used in the study.
607

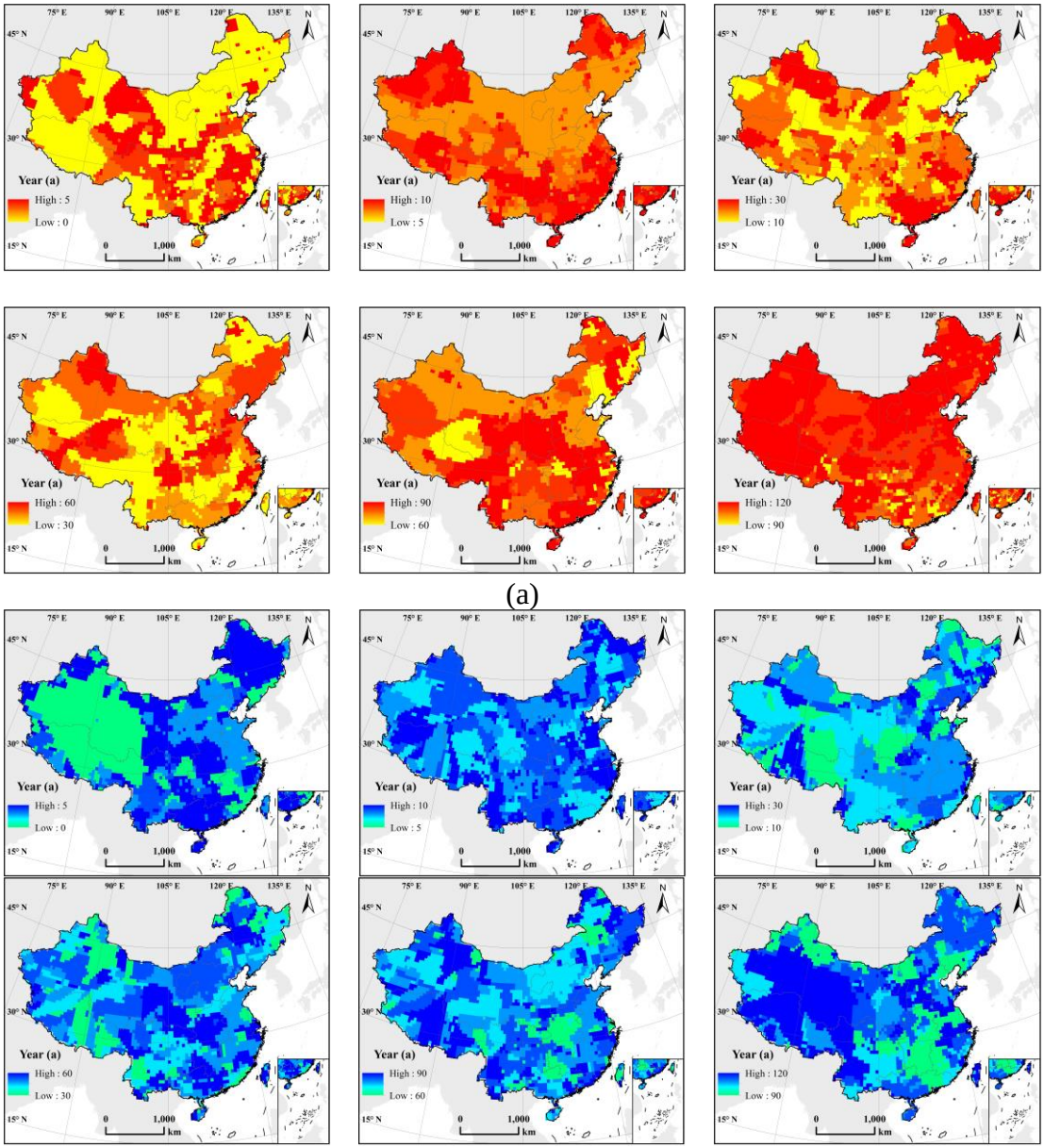

608 **Figure 5**. Grided, latitude and longitude scale distribution of (a) T and (b) P periodicity of China
609 under six periodic scales (1900–2020).
610

611

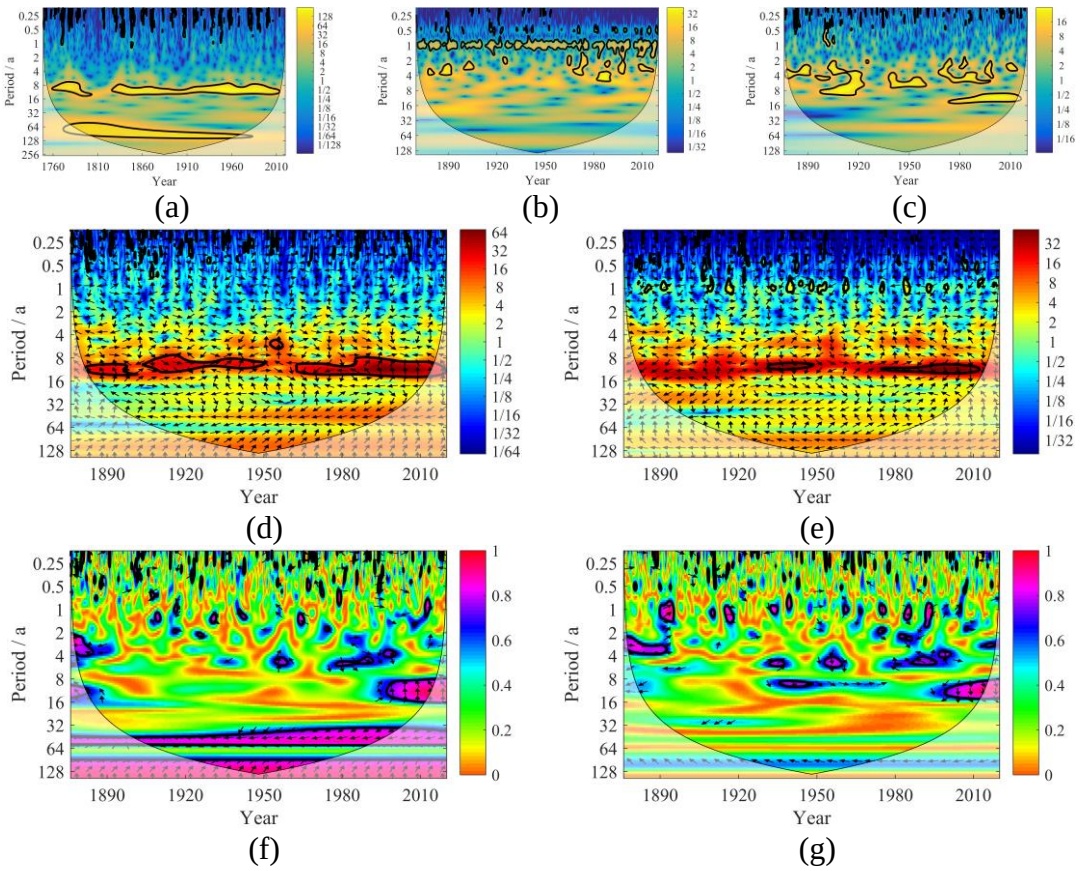

612 **Figure 6.** Continuous wavelet spectra of SN, SOI and SST (a-c). Cross wavelet transforms and
613 wavelet coherences between SN and SOI (d, f), SST (e, g). (The thin solid line represents the
614 wavelet influence cone, the thick solid line represents the horizontal interval of 5 % significance,
615 the right arrow represents the concentric phase relationship, and the left arrow represents the
616 inverse phase relationship.)
617

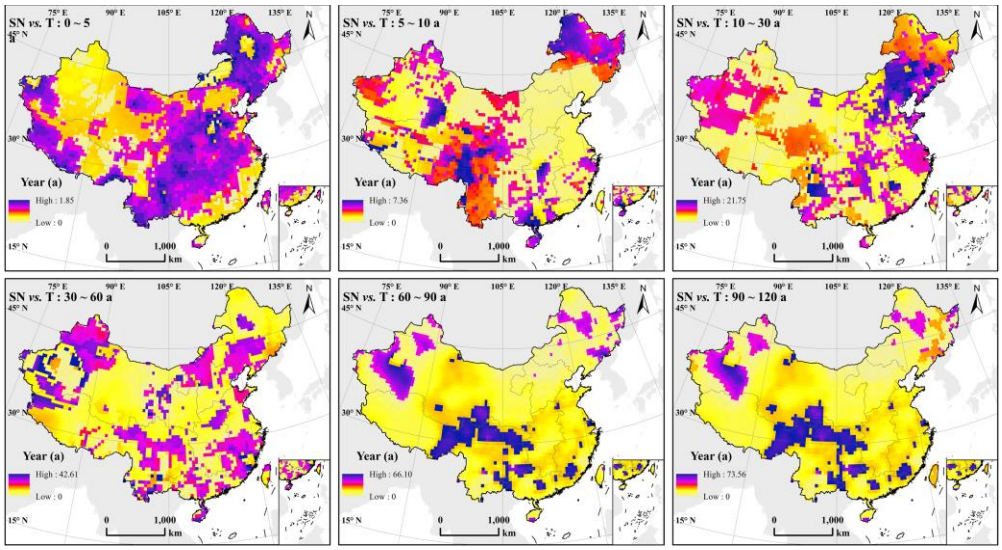
SN vs. T : 0 ~ 5
SN vs. T : 5 ~ 10 a
SN vs. T : 10 ~ 30 a
SN vs. T : 30 ~ 60 a
SN vs. T : 60 ~ 90 a
SN vs. T : 90 ~ 120 a
Year (a)
High : 1.85
High : 7.36
High : 21.75
High : 42.61
High : 66.10
High : 73.56
Low : 0
0 1,000 km

(a)

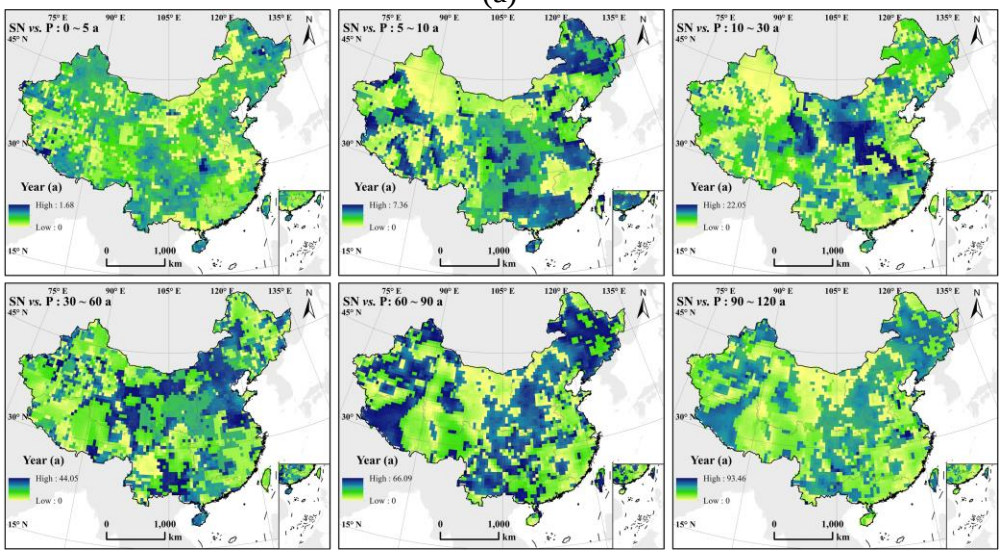
SN vs. P : 0 ~ 5 a
SN vs. P : 5 ~ 10 a
SN vs. P : 10 ~ 30 a
SN vs. P : 30 ~ 60 a
SN vs. P: 60 ~ 90 a
SN vs. P : 90 ~ 120 a
Year (a)
High : 1.68
High : 7.36
High : 22.05
High : 44.05
High : 66.09
High : 93.46
Low : 0
0 1,000 km

(b)

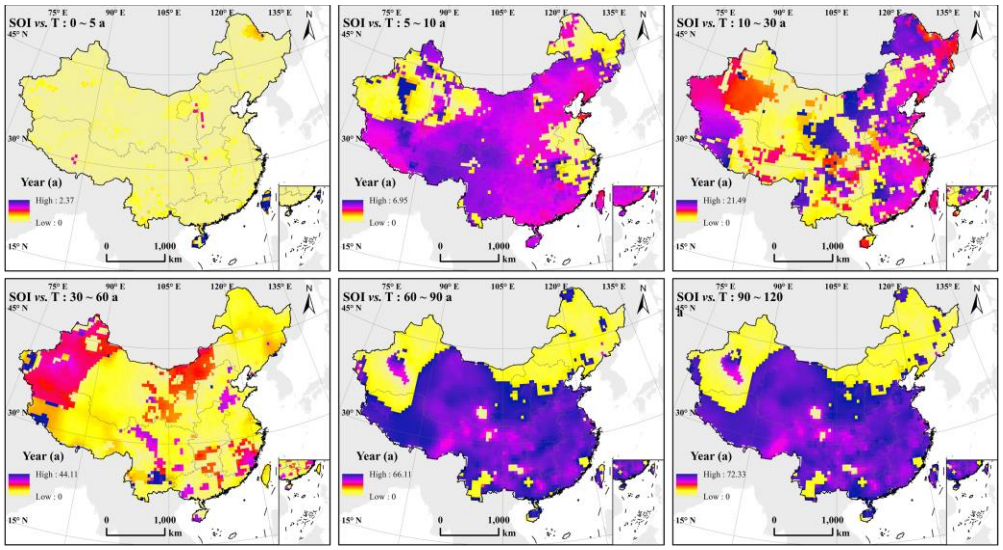
SOI vs. T : 0 ~ 5 a
SOI vs. T : 5 ~ 10 a
SOI vs. T : 10 ~ 30 a
SOI vs. T : 30 ~ 60 a
SOI vs. T : 60 ~ 90 a
SOI vs. T : 90 ~ 120 a
Year (a)
High : 2.37
High : 6.95
High : 21.49
High : 44.11
High : 66.11
High : 72.33
Low : 0
0 1,000 km

(c)

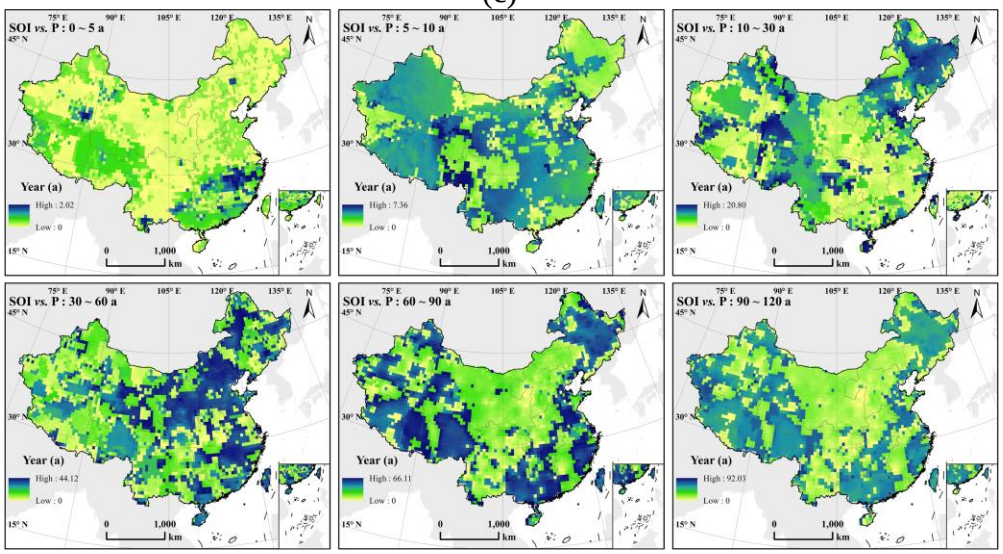
SOI vs. P : 0 ~ 5 a
SOI vs. P : 5 ~ 10 a
SOI vs. P : 10 ~ 30 a
SOI vs. P : 30 ~ 60 a
SOI vs. P : 60 ~ 90 a
SOI vs. P : 90 ~ 120 a
Year (a)
High : 2.02
High : 7.36
High : 20.80
High : 44.12
High : 66.11
High : 92.03
Low : 0
0 1,000 km

(d)

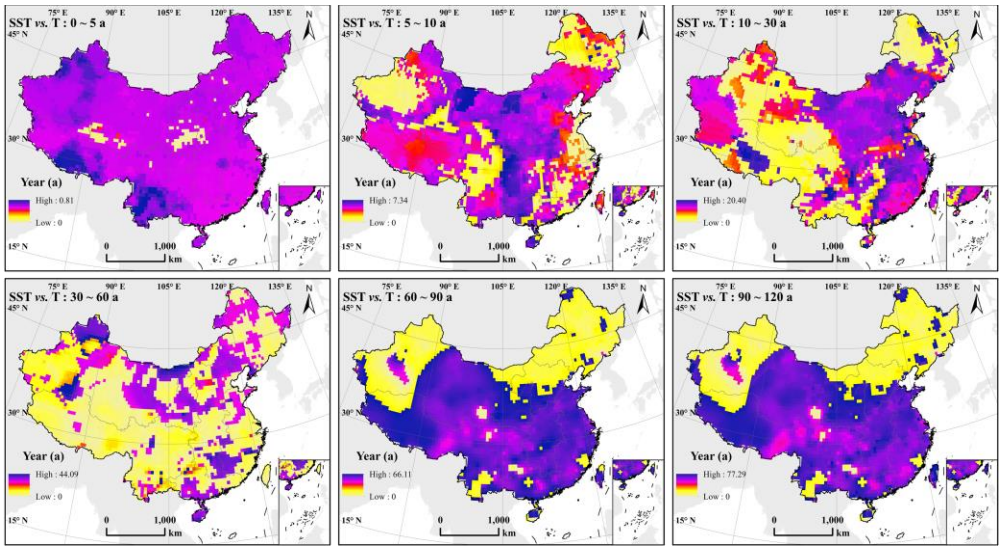

(e)

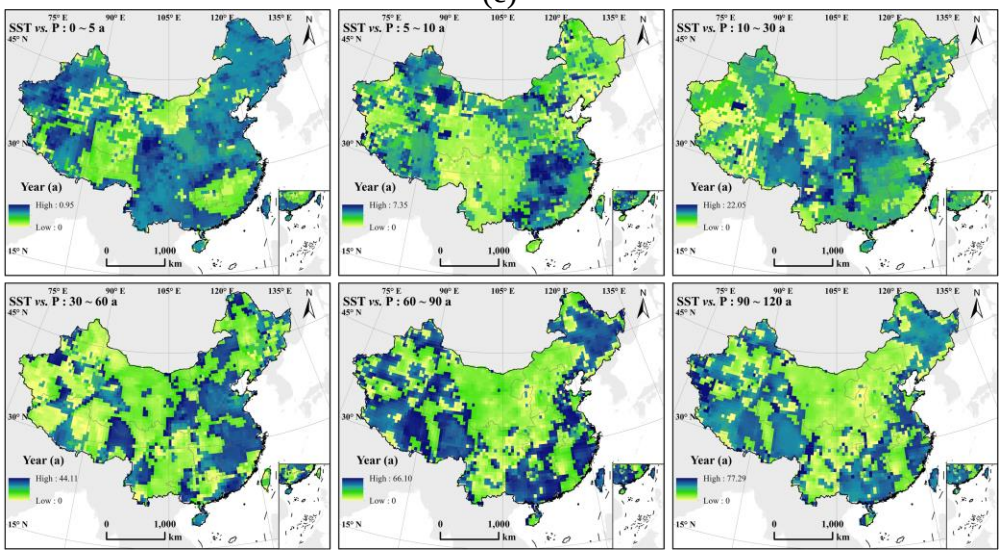

(f)

Figure 7. The significant lag period distributions of SN (a, b), SOI (c, d) and SST (e, f) to T and P of China under six periodic scales (The significance level = 0.95).

633

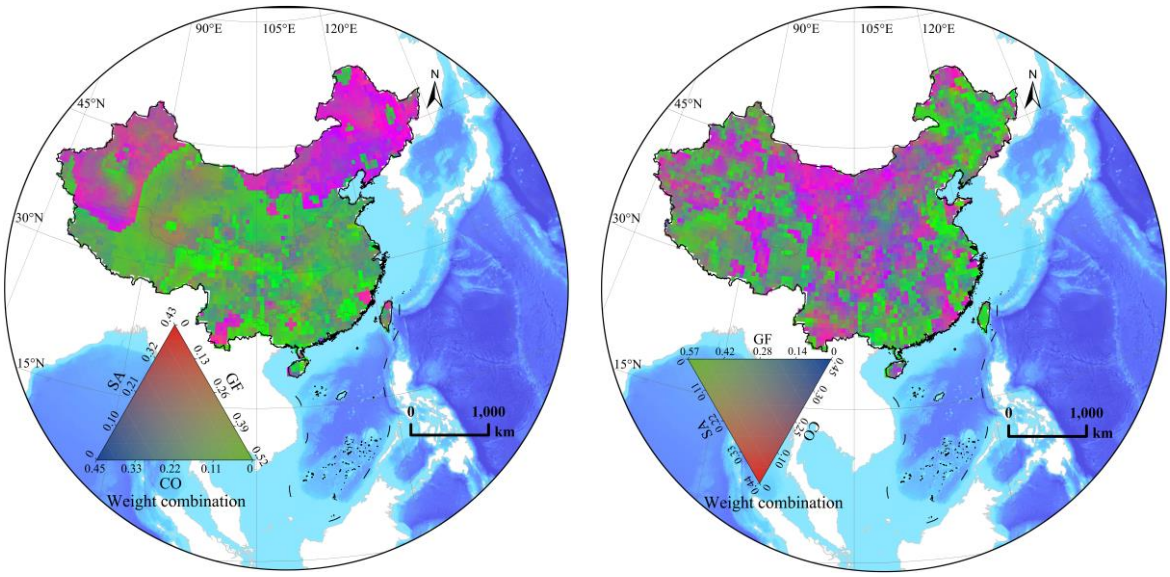

634 **Figure 8.** Entropy weight of SA, CO, and regional GF to the periodic hysteresis of T (a) and P (b)
635 under six periodic scales in China. Red, blue, and green represent SA, CO, and GF, respectively
636 (significance level = 0.95).
637

638

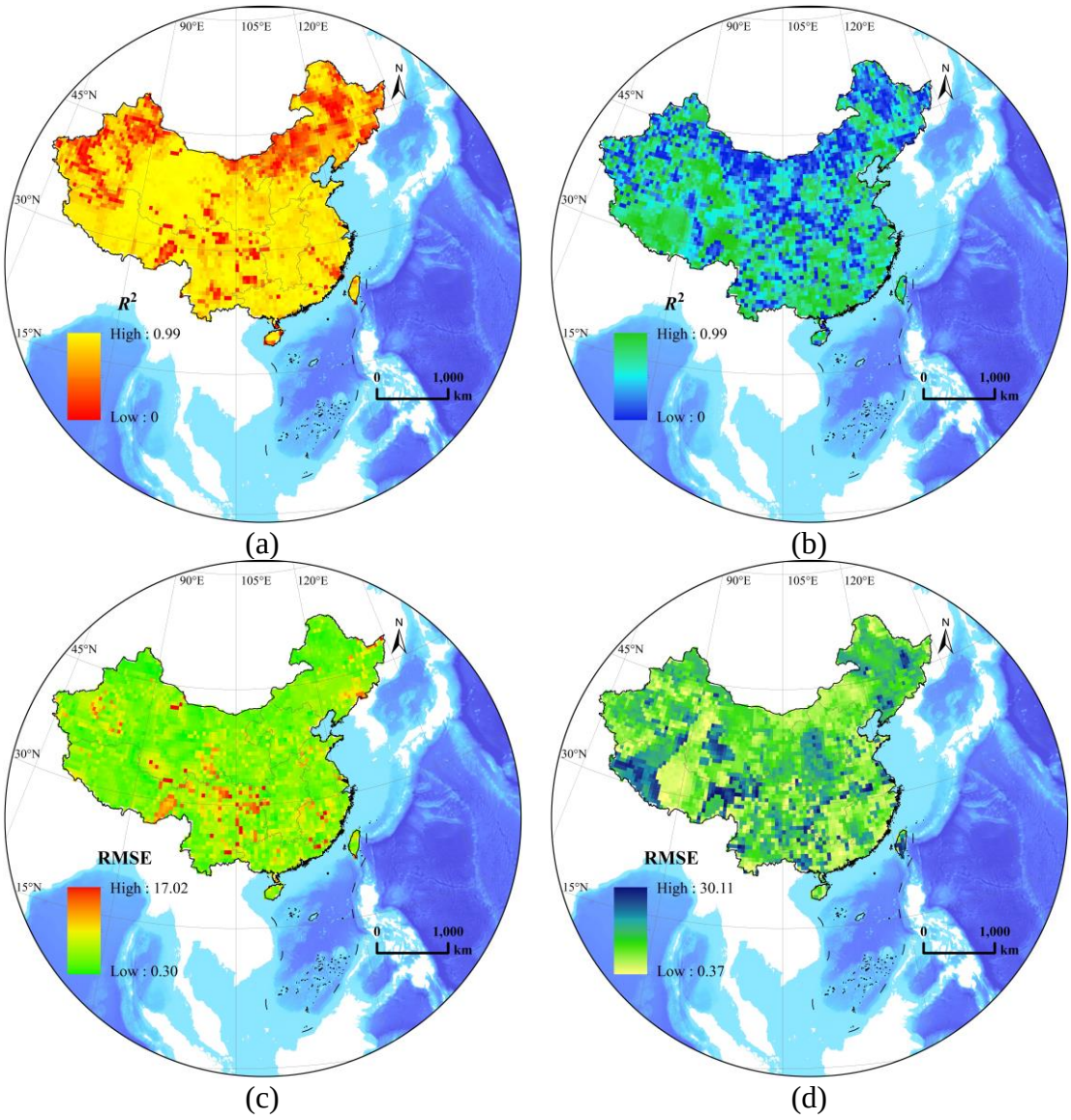

639 **Figure 9.** Accuracy (a, b) and error (c, d) analysis of simulated T (a, c) and P (b, d) hysteresis
640 period distribution using multivariate hysteretic decomposition model (MHD model; Eq.1). RMSE:
641 root mean squared error (The significance level = 0.95).
642

643

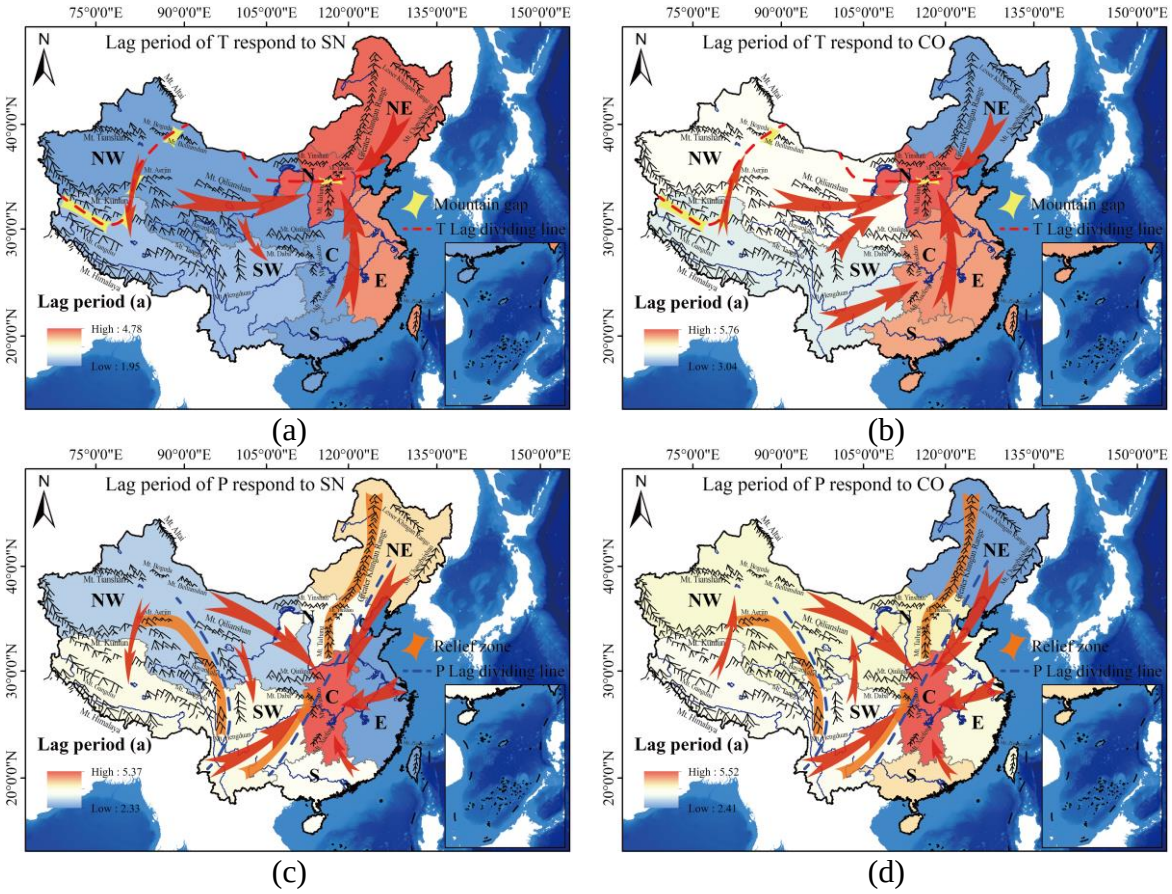

644 **Figure 10.** Theoretical diagram of the variation of (a, b) T and (c, d) P on the hysteresis period
645 distribution of (a, c) SN and (b, d) CO. NW: Northwest China; N: North China; SW: Southwest
646 China; E: Eastern China; C: Central China; S: South China.
647

Table 1. Utilized information and number of T, N, SN, SOI, SST, SEA and DEM data in the research. T: air temperature; P: precipitation; SN: sunspot number; SOI: southern oscillation index; SST: NINO 3.4 sea surface temperature; SEA: solar elevation angle; DEM: digital elevation model.

Observation Items	Longitude (°E)	Latitude (°N)	Observation Time	Number of Data
T	69.25-129.25	18.75-53.25	1900-01/2020-12	3836*1428
P	69.25-129.25	18.75-53.25	1900-01/2020-12	3836*1428
SN	-	-	1749-01/2020-12	3264
SOI	-	-	1876-01/2020-12	1740
SST	-	-	1870-01/2020-12	1812
SEA	69.25-129.25	18.75-53.25	1900-01/2020-12	3836*1428
DEM	69.25-129.25	18.75-53.25	-	3836